The Astrophysical Journal, 778:170 (14pp), 2013 December 1 doi:10.1088/0004-637X/778/2/170

THE FORMATION OF THE MASSIVE GALAXIES IN THE SSA22 $z = 3.1$ PROTOCLUSTER

M. Kubo[1], Y. K. Uchimoto[1,2,3], T. Yamada[1], M. Kajisawa[4], T. Ichikawa[1], Y. Matsuda[5], M. Akiyama[1], T. Hayashino[6], M. Konishi[2], T. Nishimura[3], K. Omata[3], R. Suzuki[3], I. Tanaka[3], T. Yoshikawa[7], D. M. Alexander[8], G. G. Fazio[9], J.-S. Huang[9], and B. D. Lehmer[10]
[1] Astronomical Institute, Tohoku University, 6-3 Aoba, Aramaki, Aoba-ku, Sendai, Miyagi, 980-8578, Japan
[2] Institute of Astronomy, University of Tokyo, 2-21-1 Osawa, Mitaka, Tokyo, 181-0015, Japan
[3] Subaru Telescope, National Astronomical Observatory of Japan, 650 North Aohoku Place, Hilo, HI 96720, USA
[4] Research Center for Space and Cosmic Evolution, Ehime University, Bunkyo-cho 2-5, Matsuyama 790-8577, Japan
[5] Chile Observatory, National Astronomical Observatory of Japan, Tokyo 181-8588, Japan
[6] Research Center for Neutrino Science, Graduate School of Science, Tohoku University, Aramaki, Aoba-ku, Sendai, Miyagi, 980-8578, Japan
[7] Koyama Astronomical Observatory, Kyoto Sangyo University, Motoyama, Kamigamo, Kita-ku, Kyoto 603-8555, Japan
[8] Department of Physics, Durham University, Durham DH1 3LE, UK
[9] Center for Astrophysics, Cambridge, MA 02138, USA
[10] The Johns Hopkins University, Homewood Campus, Baltimore, MD 21218, USA
Received 2012 September 8; accepted 2013 October 4; published 2013 November 13

ABSTRACT

We study the properties of K-band-selected galaxies ($K_{AB} < 24$) in the $z = 3.09$ SSA22 protocluster field. 430 galaxies at $2.6 < z_{phot} < 3.6$ are selected as potential protocluster members in a 112 arcmin^2 area based on their photometric redshifts. We find that ≈20% of the massive galaxies with stellar masses $>10^{11}\ M_\odot$ at $z_{phot} \sim 3.1$ have colors consistent with those of quiescent galaxies with ages >0.5 Gyr. This fraction increases to ≈50% after correcting for unrelated foreground/background objects. We also find that 30% of the massive galaxies are heavily reddened, dusty, star-forming galaxies. Few such quiescent galaxies at similar redshifts are seen in typical survey fields. An excess surface density of 24 μm sources at $z_{phot} \sim 3.1$ is also observed, implying the presence of dusty star-formation activity in the protocluster. Cross-correlation with the X-ray data indicates that the fraction of K-band-selected protocluster galaxies hosting active galactic nuclei (AGNs) is also high compared with the field. The sky distribution of the quiescent galaxies, the 24 μm sources, and the X-ray AGNs show clustering around a density peak of $z = 3.1$ Lyα emitters. A significant fraction of the massive galaxies have already become quiescent, while dusty star-formation is still active in the SSA22 protocluster. These findings indicate that we are witnessing the formation epoch of massive early-type galaxies in the centers of the predecessors to present-day rich galaxy clusters.

Key words: cosmology: observations – galaxies: clusters: general – galaxies: evolution – galaxies: formation – galaxies: high-redshift

Online-only material: color figures

1. INTRODUCTION

The formation process of massive early-type galaxies is still an important and open question. A tight color–magnitude relation has been observed for galaxies in X-ray luminous clusters at $z \sim 1$ (e.g., Ellis et al. 1997; Kodama et al. 1998; Blakeslee et al. 2003), implying that their major star formation epochs took place at $z > 2$. Since massive galaxies are the dominant populations in the central regions of rich clusters in the local universe, overdense regions in high-redshift protoclusters provide important targets for directly observing and studying the early phases of their formation.

Several protoclusters at $z > 2$ have now been identified (e.g., Steidel et al. 1998; Venemans et al. 2005; Ouchi et al. 2005; Hatch et al. 2009; Matsuda et al. 2009, 2010, 2011; Toshikawa et al. 2012) and density excesses of red massive galaxies have been reported in some systems (e.g., Kajisawa et al. 2006a; Kodama et al. 2007; Kriek et al. 2008; Uchimoto et al. 2012). Among them, the SSA22 protocluster at $z = 3.09$ is one of the most outstanding structures. The SSA22 protocluster was first discovered as a redshift spike of Lyman break galaxies (LBGs; Steidel et al. 1998) and then confirmed through the identification of a concentration of Lyα emitters (LAEs; Steidel et al. 2000; Hayashino et al. 2004; Yamada et al. 2012). The density excess of LAEs in SSA22 is ∼15 times higher than that expected from mass fluctuations at ∼50 Mpc scales (Yamada et al. 2012) and the rareness probability (i.e., the probability of finding such a rare overdensity) on 10 Mpc scales was found to be 0.0017% (Mawatari et al. 2012). Thus, the SSA22 protocluster is well characterized as a very significant density peak of galaxies at $z = 3.09$. Furthermore, overdensities of Lyα blobs (LABs; Matsuda et al. 2004), ASTE/AzTEC 1.1 mm sources (Tamura et al. 2009, 2010), and active galactic nuclei (AGNs; Lehmer et al. 2009a, 2009b) have also been reported.

In order to study how stellar mass builds up in protocluster galaxies, observations that probe rest-frame optical wavelengths are essential. Uchimoto et al. (2012, hereafter U12) conducted deep and wide-field near-infrared (NIR) observations of the SSA22 protocluster using the Subaru 8.2 m telescope equipped with the Multi-Object InfraRed Camera and Spectrograph (MOIRCS). They observed galaxies to a magnitude limit of $K_{AB} = 24$ over a 111.8 arcmin^2 area around the LAE density peak. They selected protocluster galaxy candidates using photometric redshifts and simple color criteria appropriate for distant red galaxies (DRGs; Franx et al. 2003) and Hyper Extremely Red Objects (HEROs; Totani et al. 2001). Through these selection criteria, they found that there is a significant surface number density excess of these stellar mass selected galaxies compared with those in blank fields.

Another notable discovery by U12 was the detection of "multiple merging galaxies" associated with the LABs and an ASTE/AzTEC sub-mm source. They found that multiple sub-components at $z_{\rm phot} \approx 3.1$ were clustered with separations up to 20″ (150 kpc at $z = 3.09$) within extended Lyα halos of LABs or within the beam size of the ASTE/AzTEC. This suggested that star formation is actively occurring in each sub-component before these systems undergo mergers that subsequently lead to the formation of massive galaxies. High-resolution cosmological numerical simulations show that such phenomena are indeed expected in the early phase of the formation of massive early-type galaxies (e.g., Meza et al. 2003; Naab et al. 2007).

In this paper, we investigate the properties of galaxies in the SSA22 protocluster in more detail not only by using the same MOIRCS NIR data as used in U12 but also by using *Spitzer* IRAC 3.6–8.0 μm and MIPS 24 μm data, as well as *Chandra* 0.5–8 keV X-ray data. With the IRAC data, we can constrain the spectral energy distributions (SEDs) of galaxies over a wider wavelength range, enabling us not only to obtain more accurate photometric redshifts but also to conduct improved stellar population analyses of the protocluster galaxies. We make use of the 24 μm data to constrain the dust emission and the star-formation and/or AGN activities.

Association of AGNs with the galaxies in the protocluster is also an important issue. In the SSA22 region, Lehmer et al. (2009a, 2009b) investigated the AGN hosting rate among LAEs and LBGs and found an excess AGN fraction in the protocluster over that of the field. Since there is a tight correlation between black hole mass and the spheroid stellar mass of the host galaxy in the local universe (e.g., Magorrian et al. 1998), we can investigate at what level the excess AGN fraction found in protocluster galaxies is due to an enhancement in the black hole masses of these galaxies.

The paper is organized as follows. Observations and data reduction are described in Section 2. Our techniques for selecting protocluster galaxies based on photometric redshifts are described in Section 3. In Section 4, we investigate the properties of the protocluster galaxy candidates. We discuss the detailed stellar populations of the galaxies in Section 5. In this paper, we assume cosmological parameters of $H_0 = 70$ km s^{-1} Mpc^{-1}, $\Omega_M = 0.3$, and $\Omega_\Lambda = 0.7$. $E(B-V) = 0.08$ is used for the Galactic extinction in the SSA22 field following Yamada et al. (2012). We use the AB magnitude system throughout this paper.

2. OBSERVATIONS AND DATA REDUCTION

2.1. Description of the Data

JHK_s-band images were obtained using MOIRCS on the Subaru 8.2 m telescope on 2005 June and August, 2006 July, and 2007 September (U12). The area observed with MOIRCS is located in the SSA22-Sb1 field (Matsuda et al. 2004), which covers the highest density region of LAEs at $z \approx 3.09$ (Hayashino et al. 2004; Yamada et al. 2012). The entire observed area consists of three $4' \times 7'$ fields of view (FoVs; M1, M2, and M6) and three $4' \times 3\farcm5$ FoVs (M3, M4, and M5; see also Figure 1 in U12). In total, 111.8 arcmin^2 area of the sky was observed. The data were calibrated to the UKIRT *JHK*-band photometric system (Tokunaga et al. 2002). A detailed description of the data and the reduction procedures are described in Uchimoto et al. (2008) and U12. Briefly, the limiting magnitude in the *K* band is $K = 24.1$ (5σ detection limit for a 1″.1 diameter aperture). The full width at half maximum (FWHM) of the point spread function (PSF) in the *K* band is ∼0″.5. The size of the PSF in the *J*-band is similar to that in the *K* band in the M1, M2, M3, and M6 fields, while the PSFs in the M4 and M5 fields are 0″.6 and 0″.7, respectively. Aperture photometry was performed using the PHOT task in IRAF.

Source detections were performed on the *K*-band images using SExtractor (Bertin & Arnouts 1996). Objects with 16 continuous pixels above 1.5σ of the background fluctuation were extracted. We use MAG_AUTO of SExtractor as the pseudo total magnitudes of the objects. Hereafter, this paper is focused on the sample of the *K*-band-selected galaxies with $K_{\rm AUTO} < 24$.

To supplement the *K*-band data, we use $u^\star$-band archival images taken by CFHT MegaCam (P.I. Cowie; see also Matsuda et al. 2004), the $BVRi'z'$ and the $NB497$-band images taken by Subaru Suprime-Cam (Matsuda et al. 2004; Hayashino et al. 2004), and the 3.6 μm, 4.5 μm, 5.8 μm, and 8.0 μm images taken by *Spitzer* IRAC (Webb et al. 2009). The entire field observed with MOIRCS is covered by the optical and the IRAC images. $NB497$ is a narrowband filter with a central wavelength of 4977 Å, which is used to detect Lyα emission from galaxies at $z = 3.061$–3.125. All the optical images are smoothed so that the PSF sizes are matched to be 1″.0 in FWHM. The PSF sizes of the IRAC images are ∼1″.7, slightly dependent on the wavelength. Hereafter, the IRAC 3.6 μm-band AB magnitudes are quoted using the [3.6 μm] notation; we apply the same corresponding notations to the 4.5, 5.8, and 8.0 μm bands.

We also made use of the *Spitzer* MIPS 24 μm data (Webb et al. 2009), the point source catalog of *Chandra* 0.5–8 keV data (Lehmer et al. 2009b), the archived *Hubble Space Telescope* (*HST*) Wide Field Camera 3 (WFC3) F110W and F160W data, and the Advanced Camera for Survey (ACS) F814W data (proposal ID; 11636, PI: Siana; the exposure times for each image are 2611 s for F110W and F160W, respectively, and 6144 s for F814W).

The MOIRCS field is almost entirely covered by the 24 μm data except for a ∼4 arcmin^2 region at the north west edge of the M5 field. The *Chandra* data cover the entire MOIRCS field except for the M5 region. We therefore study the X-ray properties of galaxies in the available 99.8 arcmin^2 overlapping area. The nominal limiting fluxes are $\approx 6 \times 10^{-16}$ erg cm^{-2} s^{-1} in the full band (0.5–8 keV), $\approx 2 \times 10^{-16}$ erg cm^{-2} s^{-1} in the soft band (0.5–2 keV), and $\approx 1 \times 10^{-15}$ erg cm^{-2} s^{-1} in the hard band (2–8 keV), respectively. The *HST* images cover only a few patchy regions, fewer than 10 arcmin^2 total area (for F160W), but are useful to see the structural properties of some interesting objects. The data used in this paper are summarized in Table 1.

2.2. Optical and NIR Photometry

We use photometric redshifts obtained from SED fitting to select protocluster galaxy candidates. For this purpose, we use the flux of the objects in $u^\star BVRi'z'JHK$ and IRAC 3.6 μm, 4.5 μm, 5.8 μm, and 8.0 μm bands after correcting for the effects of different PSF sizes. The flux in the optical $u^\star BVRi'z'$ bands is measured using a 2″.0 diameter circular aperture. We smoothed the *JHK*-band images to have PSF sizes of 1″.0 and then obtained 2″.0 diameter aperture fluxes. Since the IRAC images have large PSF sizes (∼1″.7 diameter), we first obtain 3″.0 diameter fluxes and then apply aperture corrections. To obtain the aperture correction factors for each object, we smoothed the *K*-band images to have PSF sizes of 1″.0 and 1″.7, to be matched with the optical and the IRAC images, respectively. For each object, the ratio of the fluxes within a 2″.0 diameter aperture on

Table 1
Data Set

Band	Instrument	Reference	Depth
J	MOIRCS/Subaru	U12	24.1–24.5[a]
H	MOIRCS/Subaru	U12	23.6–24.0[a]
K	MOIRCS/Subaru	U12	24.5–25.0[a]
$u^\star$	MegaCam/CFHT	...[b]	26.1[c]
B	Suprime-Cam/Subaru	Matsuda et al. (2004)	26.45[c]
V	Suprime-Cam/Subaru	Matsuda et al. (2004)	26.5[c]
R	Suprime-Cam/Subaru	Matsuda et al. (2004)	26.6[c]
$NB497$	Suprime-Cam/Subaru	Matsuda et al. (2004)	26.2[c]
i'	Suprime-Cam/Subaru	Hayashino et al. (2004)	26.2[c]
z'	Suprime-Cam/Subaru	Hayashino et al. (2004)	25.5[c]
3.6 μm	IRAC/*Spitzer*	Webb et al. (2009)	24.1[d]
4.5 μm	IRAC/*Spitzer*	Webb et al. (2009)	23.9[d]
5.8 μm	IRAC/*Spitzer*	Webb et al. (2009)	22.5[d]
8.0 μm	IRAC/*Spitzer*	Webb et al. (2009)	22.1[d]
24 μm	MIPS/*Spitzer*	Webb et al. (2009)	40–100 μJy[e]
0.5–8 keV	*Chandra*	Lehmer et al. (2009b)	$\approx 6 \times 10^{-16}$ erg cm^{-2} s^{-1}[f]
0.5–2 keV	*Chandra*	Lehmer et al. (2009b)	$\approx 2 \times 10^{-16}$ erg cm^{-2} s^{-1}[f]
2–8 keV	*Chandra*	Lehmer et al. (2009b)	$\approx 1 \times 10^{-15}$ erg cm^{-2} s^{-1}[f]
F160W	WFC3/*HST*	...[g]	26.7[h]

Notes.
[a] 5σ detection limiting magnitude in a 1.″1 diameter aperture.
[b] P. I. Cowie (CFHT archive).
[c] 5σ detection limiting magnitude in a 2.″0 diameter aperture on the images smoothed so that the PSF sizes are matched to be 1.″0 in FWHM.
[d] 5σ detection limiting magnitude corrected to the flux in a 1.″1 diameter aperture on the images with PSF sizes of 0.″5. Here, we adopt the average aperture correction factor of the relatively isolated sources.
[e] 3σ detection limit of the total flux in the 107.8 arcmin^2 field also observed with MOIRCS.
[f] The nominal detection limit in the 99.8 arcmin^2 field also observed with MOIRCS.
[g] P. I. Siana, Proposal ID: 11636 (in the *HST* archive).
[h] 5σ detection limiting magnitude in a 0.″6 diameter aperture.

the former image to the flux within a 3.″0 diameter aperture on the latter image was measured to obtain the correction factor.

We also use $J-K$, $i'-K$, and $K-[4.5\ \mu\mathrm{m}]$ colors of the galaxies in our analyses. The $J-K$ colors are measured from 1.″1 diameter apertures after the J and K images are smoothed so that their PSF sizes are matched with each other. If objects are not detected in the J band above a 2σ threshold, we use the 2σ values for upper limits. The $i'-K$ colors are the same as those obtained for SED fitting (see the description of the photometry above). To obtain $K-[4.5\ \mu\mathrm{m}]$ colors, we measured the 3.″0 diameter aperture flux in the IRAC images and then corrected them to the 1.″1 diameter aperture values. The aperture correction factor is the ratio of the 1.″1 aperture flux in the original K-band images to the 3.″0 aperture flux in the smoothed K-band image.

2.3. MIPS 24 μm Photometry

Since the PSF size of the 24 μm image is relatively large ($\sim$6.″0), source confusion is very significant. Therefore, we obtained 24 μm fluxes using the PSF fitting method described in Le Floc'h et al. (2005), which makes use of the DAOPHOT package in IRAF (Stetson 1987). The procedure starts by fitting a template PSF, derived using bright sources, to all the sources in the image. Next, source fluxes are estimated by subtracting the contributions from blended sources. For this task, we used the positions of objects detected in the K-band images as a prior. Fluxes were obtained using 6.″0 diameter apertures, which were aperture corrected using the PSFs derived from isolated bright sources.

Due to the inhomogeneous exposure time over the observed field, the noise level of the 24 μm image varies by position. The background noise level expected for a 6.″0 diameter aperture was estimated within $80'' \times 80''$ square regions surrounding each source. The limiting total flux (3σ) is $\approx$40–100 μJy. We use the conservative nominal detection limit of $f_{24\,\mu\mathrm{m}} = 100\,\mu$Jy to investigate the source sky distribution and their surface number density.

3. PHOTOMETRIC REDSHIFT SELECTION

3.1. Photometric Redshifts

In total, we detected $\approx$4500 objects with $K < 24$ in the SSA22 MOIRCS images (see the description of search procedure in Section 2.1). Using this catalog of sources, we identified protocluster candidates based on photometric redshifts (z_{phot}), which were measured using the following procedure.

We derived photometric redshifts for each object using the SED fitting code HyperZ (Bolzonella et al. 2000). We used the fluxes in the $u^\star BVRi'z'JHK$, 3.6 μm, 4.5 μm, 5.8 μm, and 8.0 μm bands as input to HyperZ. The fluxes used as input are the PSF-corrected values described in the previous section. For the SED templates, we used GALAXEV (Bruzual & Charlot 2003) models with a Salpeter (1955) initial mass function (IMF) and a range of metallicity from 1/100 to 1 times the solar value. The star formation histories of the templates are single burst, constant-rate continuous star formation and exponentially decaying star formation with timescales of $\tau = 0.1$–30 Gyr. We adopt the Calzetti et al. (2000) extinction law with a range of extinctions covering $E(B-V) = 0.0$–2.0. A total of $\sim$200 objects with $K < 20$ that are flagged as stars by SExtractor are removed from the sample. When the galaxies are significantly blended with adjacent objects only in the IRAC images, we obtain the photometric redshifts after excluding the IRAC data.

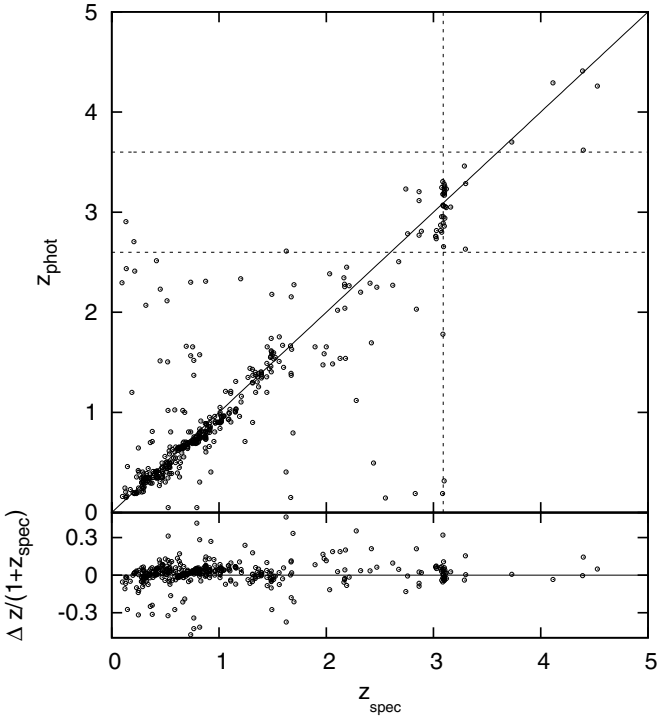

Figure 1. Top: comparison between the spectroscopic redshifts available in the NASA/IPAC Extragalactic Database and our photometric redshifts of the *K*-selected galaxies in the SSA22 field. The vertical dashed line shows the median redshift of the protocluster. The horizontal dashed lines are drawn at $z_{\rm phot} = 2.6$ and $z_{\rm phot} = 3.6$. We plot the relative errors of the photometric redshifts $\Delta z/(1 + z_{\rm spec})$ in the bottom panel, where $\Delta z = (z_{\rm spec} - z_{\rm phot})$.

In the HyperZ program, photometric redshifts are determined by the best-fit SED model based on χ^2 minimization. Objects with $\chi^2_\nu > 100$ ($\chi^2_\nu = \chi^2/\nu$; $\nu = 12$), where ν is the number of degrees of freedom, are not used in the following analysis due to the poor goodness of fit. The catastrophic failure fraction rapidly increases above this threshold. In total, we excluded 134 objects from our sample that fail this criterion; therefore, 97% of the original *K*-selected galaxy sample are included in our further analyses.

The top panel of Figure 1 shows the comparison of our photometric redshifts of *K*-selected galaxies with spectroscopic redshifts ($z_{\rm spec}$) available from the NASA/IPAC Extragalactic Database. There are 456 objects with spectroscopically confirmed redshifts. Out of these 456 objects, 33 have $z_{\rm spec} = 3.02$–3.16 and are likely protocluster sources. We excluded five known quasi-stellar objects (QSOs) and an additional three QSO-like point sources from this plot. The latter objects have not been classified as QSOs in previous studies, but their SEDs are different from the galaxy templates and more closely resemble those of QSOs. The bottom panel of Figure 1 shows the relative errors of the photometric redshifts, $\Delta z/(1 + z_{\rm spec})$, where $\Delta z = (z_{\rm spec} - z_{\rm phot})$. The standard deviation is $\langle \Delta z/(1 + z_{\rm spec})\rangle = 0.08$, excluding the galaxies with $|\Delta z|/(1 + z_{\rm spec}) > 0.5$. For galaxies at $z_{\rm spec} = 3.02$–3.16, $\langle \Delta z/(1 + z_{\rm spec})\rangle$ is 0.07. The median photometric redshift of the protocluster galaxies is $z_{\rm phot} = 3.06$, which agrees well with that of the spectroscopic sample. On the other hand, there are three catastrophic failures for the $z_{\rm spec} = 3.02$–3.16 objects. We closely inspected their SEDs and found that these three failures were likely due to the misidentifications of Lyman break and Balmer break features, a strong [O III]$\lambda\lambda$5007 emission line, and a weak Lyman break.

Table 2
Number Counts of the $K < 24$ Samples

Selection	$N_{\rm obj}$[a]	$N_{\rm obj}$[b]
ALL	4520	433(49)
DRGs	364	116(8)

Notes.
[a] Number of the objects with $K < 24$ in the MOIRCS observed field in the SSA22 field.
[b] Number of the galaxies with $K < 24$ and $2.6 < z_{\rm best} < 3.6$ ($2.6 < z_{\rm spec} < 3.6$).

In U12, the photometric redshifts were obtained with $\langle \Delta z/(1 + z_{\rm spec})\rangle = 0.12$ for all the *K*-selected galaxies and $\langle \Delta z/(1 + z_{\rm spec})\rangle = 0.08$ for those at $z_{\rm spec} \approx 3.09$. We have thus improved the photometric redshift measurements over those provided by U12.

In the following analyses, we define our best redshift measurement, $z_{\rm best}$, as the spectroscopic redshift when it is available; otherwise, we adopt the photometric redshift as $z_{\rm best}$. In total, we select 433 *K*-selected galaxies at $2.6 < z_{\rm best} < 3.6$, which may contain a significant fraction of protocluster galaxies at $z \approx 3.09$. A breakdown of the number of *K*-selected galaxies with spectroscopic and photometric redshifts is shown in Table 2. Note that we removed 10 objects that are blended with nearby very bright objects in the optical images.

3.2. The Redshift Distribution of the K-selected Galaxies

The left panel of Figure 2 shows the $z_{\rm best}$ distributions of the *K*-selected galaxies in the SSA22 field. For comparison, we also plot the redshift distribution of the *K*-selected GOODS-North (GOODS-N) galaxies from the MOIRCS Deep Survey (MODS) catalog (Kajisawa et al. 2006b, 2011). In this comparison, the number of galaxies in GOODS-N has been normalized to the area of the SSA22 survey field. MODS obtained photometric redshifts of the galaxies with $K < 25.1$ (5σ detection limit) in a 103.3 arcmin^2 area. The rms error of the photometric redshifts are $\langle \Delta z/(1 + z_{\rm spec})\rangle \sim 0.12$ for the whole sample and $\sim$0.08 for the sample at $z \sim 3$ after clipping the catastrophic failures with $|\Delta z|/(1 + z_{\rm spec}) > 0.5$ (Ichikawa et al. 2007). Note that the rms error of the photometric redshifts in the SSA22 field is comparable to that of MODS but contains more catastrophic failures. That is, $\approx$1% of the objects at $z_{\rm spec} < 2$ in our SSA22 catalog are contaminants at $2.6 < z_{\rm phot} < 3.6$, while the equivalent contaminant fraction for the MODS is $\sim$0.2%. The entire redshift distributions agree well while there is a notable excess in the number of $z \sim 3$ sources in the SSA22 field.

The right panel of Figure 2 shows the $z_{\rm best}$ distributions of DRGs, which are selected using the color criterion $J - K > 1.4$. DRGs are thought to be dust-obscured, star-forming galaxies and/or relatively old passive galaxies with significant Balmer or 4000 Å breaks at $2 < z < 4$ (Franx et al. 2003). Spectroscopic observations show that objects identified as DRGs with $K > 21$ are indeed dominated by galaxies at $z > 2$ (e.g., Wuyts et al. 2007; Kajisawa et al. 2011). DRGs in both SSA22 and GOODS-N are dominated by galaxies at $z_{\rm best} > 2$. In SSA22, we detected 364 DRGs among the entire galaxies with $K < 24$ and 118 of them are at $2.6 < z_{\rm best} < 3.6$. From Figure 2, it is clear that there is an excess number density of DRGs in SSA22 compared with GOODS-N over a wide range of redshift. The density excess at $2 < z < 4$ is likely to be caused by the excess number of galaxies in the $z = 3.09$ protocluster. Indeed, five of the

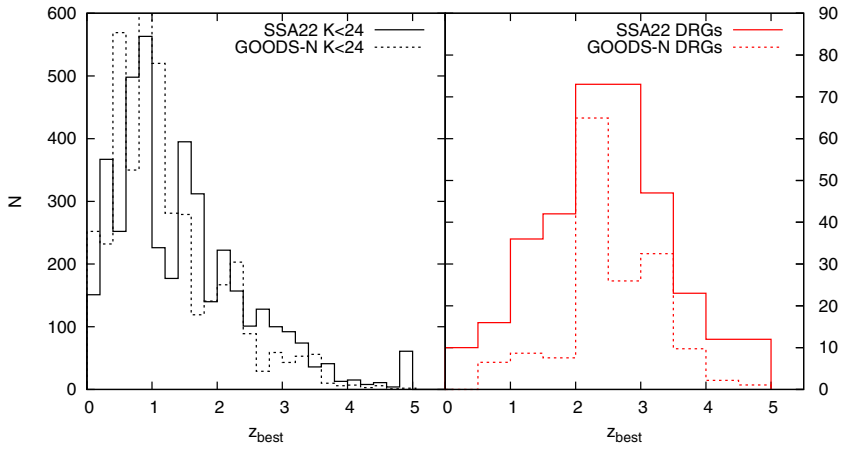

Figure 2. Left: the $z_{\rm best}$ distributions of the K-selected galaxies. All the galaxies with $K < 24$ are plotted. The black solid line is the redshift distribution of the K-selected galaxies in the SSA22 field and the dashed line is that in the GOODS-N field. Right: the $z_{\rm best}$ distributions of the DRGs with $K < 24$. The red solid line is the redshift distribution of the DRGs in the SSA22 field and the dashed line is that in the GOODS-N field.

(A color version of this figure is available in the online journal.)

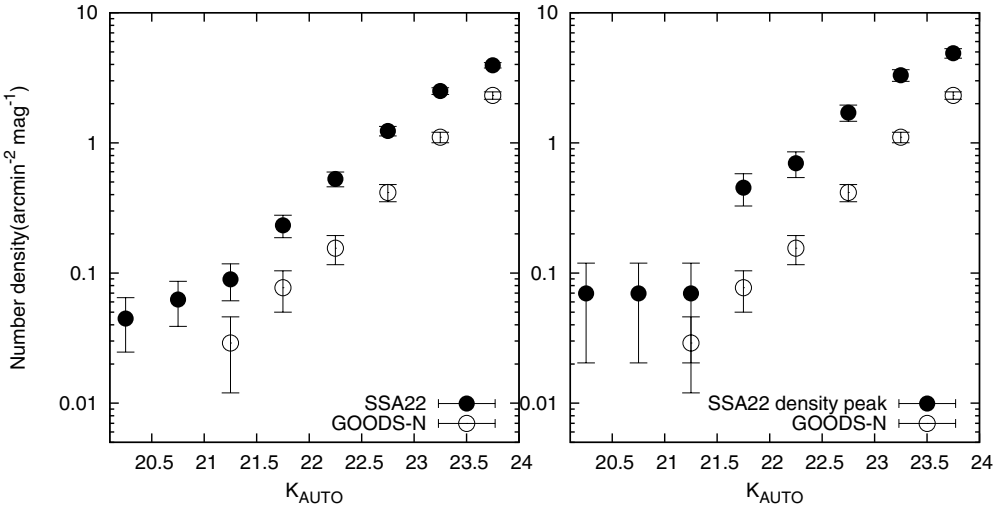

Figure 3. Left: the cumulative surface number density of K-selected galaxies at $2.6 < z_{\rm best} < 3.6$. The black filled circles are objects in the entire SSA22 field and the black open circles are objects in the GOODS-N field. Right: similar to the left panel but the black filled circles are the cumulative surface number density at the SSA22 highest density region.

nine DRGs in SSA22 with known spectroscopic redshifts are at $3.09 < z_{\rm spec} < 3.12$. The density excess at $z < 2$ may be due to a true overdensity at $1 < z < 2$; however, it is possible that high-redshift ($z > 2$) contaminants with catastrophic photometric redshift failures may contribute to the low-redshift overdensity. The scatter of photometric redshift is generally larger for the featureless reddened spectra.

3.3. The Density Excess of the K-selected Galaxies at $2.6 < z_{\rm best} < 3.6$

In this subsection, we discuss further the surface number density excess of the K-selected galaxies at $2.6 < z_{\rm best} < 3.6$ in the SSA22 field. Note that the excess of the purely color-selected DRGs (i.e., no photometric redshift selection) was previously reported by U12.

In the left panel of Figure 3, we show the cumulative surface number density of the K-selected galaxies at $2.6 < z_{\rm best} < 3.6$ in the entire SSA22 field. The error bar in each bin corresponds to the 1σ Poisson error. We also plot the distribution in GOODS-N for comparison. The surface number density of the galaxies with $K < 24$ in the SSA22 field is 3.87 ± 0.19 arcmin^{-2}, which is 1.7 times that in GOODS-N. If we subtract the contribution of field galaxies (based on GOODS-N) from the SSA22 number counts, we estimate that there is an excess of $\approx$180 K-selected galaxies, potentially sources that are members of the protocluster.

We identified the position of the large-scale density peak of the K-selected galaxies at $2.6 < z_{\rm best} < 3.6$ on the sky by smoothing the galaxy distribution with a Gaussian kernel of scale $\sigma = 0.5$ arcmin. We found the location of the peak at $(\alpha, \delta) \approx (22^{\rm h}17^{\rm m}20^{\rm s}, +00^\circ17'.7)$, which is shown in Figure 6. Interestingly, the location of the peak is within 1 arcmin of the peak of the $z = 3.09$ LAE distribution, which was obtained using a smoothing scale of 1.5 arcmin in Yamada et al. (2012). The density peak of the simple color-selected DRGs was also found to be near that of the protocluster LAEs (U12). The right panel of Figure 3 shows the cumulative surface number density of K-selected galaxies at $2.6 < z_{\rm best} < 3.6$ within a 1.5 Mpc radius around the density peak. We find the density of $K < 24$ galaxies in this region of SSA22 to be 2.1 times that found in the GOODS-N field.

In order to test whether the K-selected source overdensity in SSA22 over GOODS-N was due to differences in the accuracy of the photometric redshifts, we performed simulations. While

the rms errors after clipping the outliers are comparable, there are more catastrophic failures ($|\Delta z| \gtrsim 0.5$) in the SSA22 sample. We evaluated the relative fraction of the catastrophic failures in the SSA22 sample compared with the MODS sample by constructing mock catalogs where the distributions of the parameters in SED fitting are similar to those in the MODS sample. We added photometric errors to the mock catalog sources and obtained the fraction of catastrophic failures. In this process, the mock photometric error distribution was matched with that obtained for the SSA22 galaxies. After 100 realizations, we found that 1.0 ± 0.2% of the galaxies at $z_{\rm model} < 2$ are contaminated by the $2.6 < z_{\rm phot} < 3.6$ sample in the mock catalogs. This contamination fraction is only 0.2% for the real MODS catalog. This implies that at most ∼1.1 times the surface number density excess can be attributed to contamination due to the catastrophic redshift measurements. Thus, the density excess of *K*-selected galaxies at $2.6 < z_{\rm phot} < 3.6$ in the SSA22 field is not caused by artifacts due to accuracy differences in the photometric redshifts.

U12 reported that the surface number density of the pure color-selected DRGs (i.e., without photometric redshift constraint) is 1.8–2.1 times that in the general field. To extend their analysis, we computed the number density of DRGs with $2.6 < z_{\rm best} < 3.6$. We corrected the detection completeness of the DRGs in the M4 and M5 fields where the images are slightly shallow due to the relatively large PSF sizes. The correction factors at the faintest bins are found to be ≈1.1. After applying these corrections, we obtained the surface number density of the DRGs at $2.6 < z_{\rm best} < 3.6$. At $K < 24$, we find a surface density of 1.04 ± 0.10 arcmin^{-2}, which is 2.5 times that found in GOODS-N. This excess increases to a factor of 2.7 near the *K*-selected source density peak.

Overdensities of red galaxies in protoclusters at $z \sim 2$ have also been found in other studies (e.g., Kodama et al. 2007; Zirm et al. 2007; Doherty et al. 2010). On the other hand, no significant density excesses of the DRG-like objects were observed in some protoclusters at $z \sim 3$, including MRC 0943-242 at $z = 2.93$ (Doherty et al. 2010) and MRCS0316-257 at $z = 3.13$ (Kuiper et al. 2010; based on Balmer-break selection of galaxies with colors similar DRGs). Kuiper et al. (2010) noted that it is difficult to detect the surface number density excess of DRGs with their sample due to limited area and depth. We note that our NIR data in the SSA22 field are wider and deeper than those used by Doherty et al. (2010) and Kuiper et al. (2010).

A density excess of 24 μm-detected galaxies at $2.6 < z_{\rm best} < 3.6$ was also found to be 1.9 times that of GOODS-N. As we will discuss below, the 24 μm-detected galaxies at $z \sim 3$ are likely to be heavily dust obscured star-forming galaxies and/or AGNs. At such high redshifts, the 24 μm detection limit corresponds to a star formation rate (SFR) of several 100–1000 $M_\odot$ yr^{-1}. The density excess of 24 μm sources around high-redshift radio sources (HzRGs) has been reported in other fields. For example, Mayo et al. (2012) reported an average overdensity of 2.2 ± 1.2 of 24 μm sources (<0.3 mJy) using simple source counts within 1.′75 radius regions around HzRGs at $1 \leqslant z \leqslant 5.2$. Also, Tanaka et al. (2011) reported a density excess around an HzRG at $z = 2.48$.

4. PROPERTIES OF *K*-SELECTED GALAXIES AT $2.6 < z_{\rm best} < 3.6$

In this section, we investigate the properties of the *K*-selected galaxies with redshifts $2.6 < z_{\rm best} < 3.6$. For our purposes here, we compute stellar masses and SFRs for these galaxies assuming they are members of the protocluster and located at $z = 3.09$. With these assumptions, we repeated the SED fitting analysis described in the previous section with the fixed redshift, $z = 3.09$.

4.1. Star Formation Rates

We estimated SFRs for the galaxies using extinction-corrected, rest-frame ultraviolet (UV). We converted 1500–2800 Å luminosities to $\rm SFR_{UV}$ values following (Kennicutt 1998)

$$\rm SFR_{UV}\ (\mathit{M}_\odot\ yr^{-1}) = 1.4 \times 10^{-28}\, \mathit{L}_\nu\ (erg\ s^{-1}\ Hz^{-1}).$$

The conversion factor 1.4×10^{-28} was obtained assuming a Salpeter IMF over the stellar mass range of 0.1–100 $M_\odot$, a constant continuous star formation history, and stellar ages older than 10^8 yr. Since the typical age of LBGs at $z \simeq 3$ is estimated to be 10^8–10^9 yr assuming a constant continuous star formation model (e.g., Pettini et al. 2001), the use of this equation in our study is appropriate. We estimate the rest-frame UV luminosities at ∼1900 Å from their total magnitudes in the i'-band. The extinction-corrected SFR values, $\rm SFR_{UV,corr}$, are obtained by adopting the $E(B-V)$ value of the best-fit SED models. Note that the true conversion factor can be smaller for younger galaxies that do not reach equilibrium between the birth and death of their massive stars.

The SFR can also be estimated using the 24 μm flux, however, Elbaz et al. (2010) point out that using the 24 μm data alone results in a significant overestimation of the SFR for galaxies with $L_{\rm IR} > 10^{12}\ L_\odot$ at $z = 1.5$–2.5. The limiting flux at 24 μm for our observations and high-redshift sample corresponds to such a high luminosity limit. Elbaz et al. (2010) also reported that $L_{\rm IR}$ can be overestimated by an order of magnitude if a luminous AGN is present. In fact, 10 out of the 31 24 μm detected galaxies at $2.6 < z_{\rm best} < 3.6$ are also detected by *Chandra*, which indicates that contributions from AGNs cannot be ignored. We therefore choose to use only $\rm SFR_{UV,corr}$ when estimating SFRs for our sample. We found that 21 *K*-selected galaxies had very high SFRs ($\rm SFR_{UV,corr} \sim$ 1000–10000 $M_\odot$ yr^{-1} and $E(B-V) > 0.5$), but were not detected at 24 μm. In the following analyses, we reject these sources from our sample, since they are likely to be low-redshift contaminants.

The range, average, and median of the $\rm SFR_{UV,corr}$ values of the *K*-band-detected galaxies at $z_{\rm spec} \approx 3.09$ in the SSA22 field are ∼10–730 $M_\odot$ yr^{-1}, 122 $M_\odot$ yr^{-1}, and 41$M_\odot$ yr^{-1}, respectively. This is consistent with the sample from Magdis et al. (2010), who studied LBGs with a similar range of stellar masses at $z_{\rm spec} \sim 3$.

4.2. Stellar Masses

We estimated stellar masses for our galaxies using their best-fit SEDs and *K*-band total magnitudes. Our sample is nearly complete for galaxies with stellar masses $>10^{10.5}\ M_\odot$ independent of their SEDs. Figure 5 shows the stellar mass and $\rm SFR_{UV,corr}$ distributions of the *K*-selected galaxies and DRGs at $2.6 < z_{\rm best} < 3.6$ in the SSA22 field.

Since we study galaxies at $z \approx 3.09$, some systems will have contributions from the [O III]λλ5007 emission line falling in the *K* band. Assuming the conversion factor of the Hα line luminosity to SFR from Kennicutt (1998), a line ratio of Hα to Hβ of 2.75 (Osterbrock 1989), a Hβ to [O III] ratio of ∼0.3–3 (Moustakas & Kennicutt 2006), and moderate extinction $E(B-V) \lesssim 0.1$, the expected flux of the [O III]

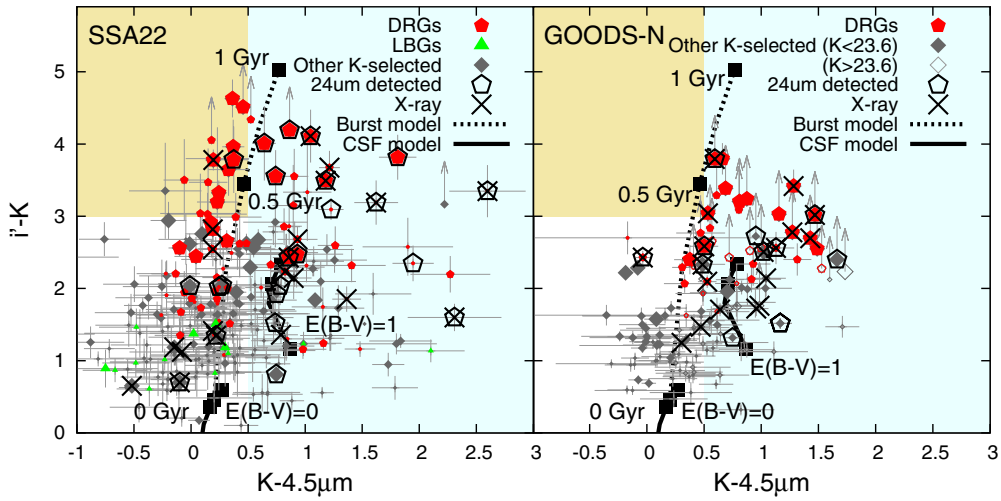

Figure 4. $i' - K$ versus $K - [4.5\,\mu\mathrm{m}]$ two color diagram of the K-selected galaxies at $2.6 < z_{\mathrm{best}} < 3.6$ in the SSA22 (left) and GOODS-N (right) fields. The gray filled diamonds are all the K-selected galaxies that are also detected in $[4.5\,\mu\mathrm{m}]$. The size of the symbols reflects the stellar masses of the objects classified as $M_{\mathrm{star}} < 10^{10.5}\,M_{\odot}$ (small), $10^{10.5}\,M_{\odot} < M_{\mathrm{star}} < 10^{11}\,M_{\odot}$ (medium), and $M_{\mathrm{star}} > 10^{11}\,M_{\odot}$ (large). The red filled pentagons and the green filled triangles are the K-selected galaxies at $2.6 < z_{\mathrm{best}} < 3.6$ classified as DRGs and LBGs, respectively. The open black pentagons are the galaxies detected in 24 μm and the black crosses are those detected in *Chandra* full- and/or soft- and/or hard-bands. The black dotted line and square points are the color evolution track with age for a single burst star formation model at $z = 3.1$. The square points are at 0, 0.5, and 1.0 Gyr, from bottom to top. The black solid lines and square points are those for a constant continuous star formation model with $E(B-V) = 0$ (the 0 Gyr point is out of the range of the figure) and 1. We classified the galaxies in the yellow region as "quiescent galaxies" ($i' - K > 3.0$ & $K - [4.5\,\mu\mathrm{m}] < 0.5$), in the light cyan region as "dusty starburst galaxies" ($K - [4.5\,\mu\mathrm{m}] > 0.5$), and in the unshaded region as "normal star-forming galaxies" ($i' - K < 3$ and $K - [4.5\,\mu\mathrm{m}] < 0.5$). In the GOODS-N field, an F775Wdetection limit of $i_{775} = 25.6$ (5σ limit) is used. Therefore, we plot the galaxies fainter than $K_{\mathrm{AUTO}} = 23.6$ with open symbols in GOODS-N.

(A color version of this figure is available in the online journal.)

emission line of a galaxy with SFR $\sim 50\,M_{\odot}$ yr^{-1} at $z \sim 3$ is $\sim 10^{-16}$–10^{-17} erg cm^{-2} s^{-1}. Such [O III] intensities provide a non-negligible contribution ($\lesssim$0.5 mag) to the measured K-band fluxes for $z = 3.0$–3.2 galaxies near the faint end of our sample ($K \simeq 23$–24). Empirically, the rest-frame equivalent widths of [O III]$\lambda\lambda$5007 emission lines have values up to $\sim$1000 Å (Kakazu et al. 2007; Atek et al. 2011). However, the actual strength of [O III] emission lines for the various type of galaxies at $z \sim 3$ remains uncertain and it is beyond the scope of this paper to robustly evaluate the effect for each individual object.

4.3. Rest-Frame UV-to-NIR Colors

Figure 4 shows the $i' - K$ versus $K - [4.5\,\mu\mathrm{m}]$ color–color diagram for K-selected galaxies with $2.6 < z_{\mathrm{best}} < 3.6$ in the SSA22 and GOODS-N fields. This diagram has been used in past studies to distinguish between star-forming and quiescent galaxies at $z > 2$. For example, Labbé et al. (2005) and Papovich et al. (2006) studied $z > 2$ DRGs in the Hubble Deep Field-South and GOODS-South (GOODS-S) field, respectively. For the SSA22 sample, we show the 268 K-selected galaxies at $2.6 < z_{\mathrm{best}} < 3.6$ that are detected in the 4.5 μm and do not suffer from source blending with nearby sources. The detection limit at 4.5 μm after applying aperture corrections is $\approx$23.9 (5σ limit).

We classified galaxies by comparing their $i' - K$ versus $K - [4.5\,\mu\mathrm{m}]$ colors with simple synthetic models. We classified galaxies with $i' - K > 3.0$ and $K - [4.5\,\mu\mathrm{m}] < 0.5$ as quiescent galaxies, since these colors are consistent with those expected for galaxies with single-burst ages >0.5 Gyr. Galaxies with $K - [4.5\,\mu\mathrm{m}] > 0.5$ were classified as heavily dust-obscured starburst galaxies, since these colors are consistent with those expected for galaxies with constant continuous star formation history with $E(B-V) \sim 1$. Finally, the star-forming galaxies with moderate dust obscuration are expected to distribute throughout the region with $i' - K < 3.0$ and $K - [4.5\,\mu\mathrm{m}] < 0.5$. We indicate the DRGs and LBGs (Steidel et al. 2000) in Figure 4. The DRGs span a wide range of colors and dominate the population of the reddest galaxies in $i' - K$. On the other hand, LBGs are typically blue in $i' - K$ and correspond to star-forming galaxies with moderate extinction. There are some very red objects in $K - [4.5\,\mu\mathrm{m}] \gtrsim 1.5$ that could be AGNs with power-law spectra in the NIR (e.g., Donley et al. 2007; Yamada et al. 2009).

We carefully checked the observed SEDs of the quiescent galaxy candidates since their red colors could be due to the presence of strong [O III]$\lambda\lambda$5007 emission lines (see the discussion above). Indeed, 4 out of the 15 candidates show clear excesses in the K band only; they are typically $\sim$0.3 mag redder in $H-K$ and $\sim$0.4 mag bluer in $K - [3.6\,\mu\mathrm{m}]$ than the average colors of the remaining 11 objects. All of these 4 galaxies are fainter than $K = 23$. The SEDs of the remaining 11 objects, on the other hand, are well fit by the models of quiescent galaxies with ages of 0.5–2 Gyr at $z = 3.1$. If we consider only galaxies with $K < 23$, we find a corresponding $2.6 < z_{\mathrm{best}} < 3.6$ quiescent galaxy surface density of 0.10 ± 0.03 arcmin^{-2} in SSA22. All of these quiescent galaxies satisfy the DRG color selection criterion in $J-K$, suggesting the presence of significant Balmer or 4000 Å breaks. On the other hand, $\approx$20% of the DRGs with $K < 23$ at $2.6 < z_{\mathrm{best}} < 3.6$ in SSA22 lie in the color range of quiescent galaxies.

There is one quiescent galaxy that is detected in 24 μm. However, the SED of this object is also well fit by a model of passive evolution with an age of 1.7 Gyr at $z \approx 3.09$, with a slight excess over the model at >5.8 μm. The observed light at wavelengths shorter than 4.5 μm is dominated by the old stellar component, while the mid-infrared emission maybe due to dust heated by an AGN. For the remaining 10 objects without

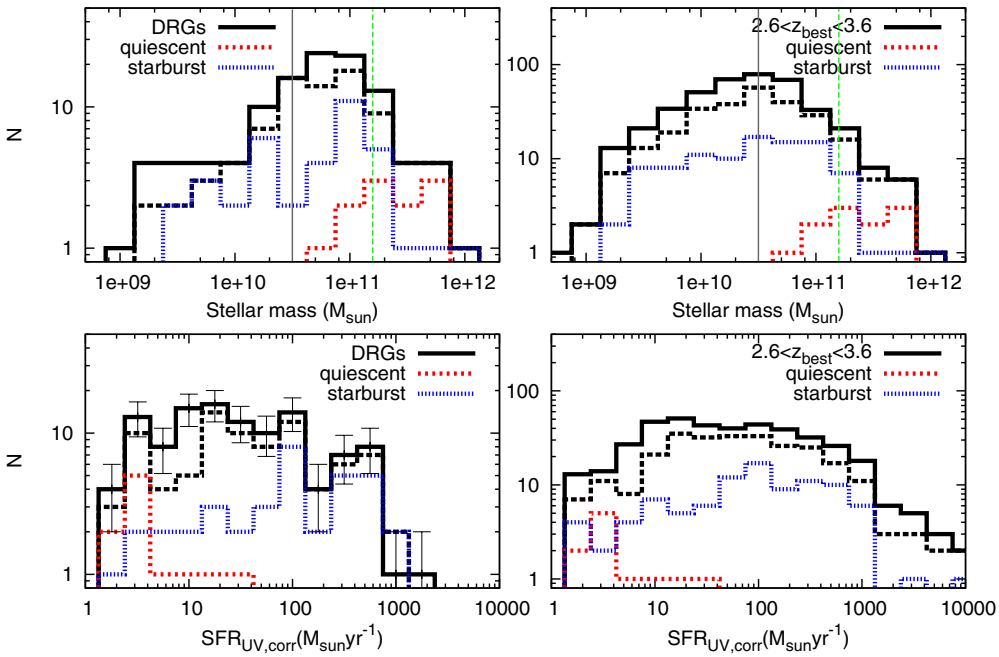

Figure 5. Top-left panel: the stellar mass distribution of the DRGs at $2.6 < z_{\rm best} < 3.6$. The solid black line is the stellar mass distribution of all the DRGs at $2.6 < z_{\rm best} < 3.6$ and the dashed black line is that of the DRGs also detected in [4.5 μm], which are plotted in Figure 4. The red and blue dashed lines are the stellar mass distribution of the DRGs classified as quiescent galaxies and dusty starburst galaxies, respectively. The gray solid line is the stellar mass limit for typical K-selected galaxies with $K = 24$ at $z = 3.1$. The green dashed line is that for quiescent galaxies, which are galaxies with a burst-like star formation history with ages of 0.5–2 Gyr, with $K = 23$ at $z = 3.1$. Bottom-left panel: the $\rm SFR_{UV,corr}$ distribution of the DRGs. Top-right and bottom-right panels: the stellar mass and $\rm SFR_{UV,corr}$ distribution of the K-selected galaxies at $2.6 < z_{\rm best} < 3.6$.

(A color version of this figure is available in the online journal.)

24 μm detections, we stacked their 24 μm images and found no significant stacked detection. The corresponding upper limit of the 24 μm flux for the stacked sources is 17 μJy (2σ).

Figure 5 shows the stellar mass and $\rm SFR_{UV,corr}$ distributions of the quiescent galaxies. Note that the $\rm SFR_{UV,corr}$ of quiescent galaxies are just upper limits, since these are obtained with the assumption that the UV light of the galaxies is dominated by massive young stars (see the discussion in Section 4.1). The $\rm SFR_{UV,corr}$ upper limits of the quiescent galaxies are typically less than 10 $M_\odot$ yr^{-1}, which is significantly lower than the average value for LBGs at $z \sim 3$ (see, e.g., Shapley et al. 2003 and Magdis et al. 2010 for other samples of LBGs).

The stellar masses of the quiescent galaxies span the range of $10^{10.8-11.7}$ $M_\odot$, comparable to those of local, massive, early-type galaxies. On the other hand, ≈20% (9/43) of the K-selected galaxies with stellar masses $>10^{11}$ $M_\odot$ at $2.6 < z_{\rm best} < 3.6$ in SSA22 are classified as quiescent sources.

The deficit of quiescent galaxies below $\sim 10^{11}$ $M_\odot$ is likely to be a selection effect. Our burst models for galaxies with ages in the range of 0.5–2 Gyr have larger stellar mass-to-light ratios than typical K-selected galaxies at $z \sim 3$. Therefore, the limit of $K = 23$ corresponds to $\sim 10^{11} M_\odot$ (the dashed green line in Figure 5). As discussed above, while we attempted to select quiescent galaxies as faint as $K = 24$, all of those with $K = 23$–24 are likely to be [O III] emitters.

The presence of these quiescent galaxies in the SSA22 field is conspicuous. With the same color criterion and detection limits, we found no such quiescent galaxies at $2.6 < z_{\rm best} < 3.6$ in the MODS GOODS-N sample. Furthermore, few DRGs in GOODS-S field satisfy our selection criterion for quiescent galaxies (Papovich et al. 2006) despite having a broader redshift range for selection. If we correct the number of the foreground/background galaxies, adopting the factor of 1.8 density excess of the protocluster field (Table 3), the fraction of quiescent galaxies among the K-band-selected galaxies with stellar masses $>10^{11} M_\odot$ is expected to be at most ≈50% (i.e., 9/19).

On the other hand, 96 of the K-selected galaxies at $2.6 < z_{\rm best} < 3.6$ were classified as dusty starburst galaxies ($K - [4.5\,\mu{\rm m}] > 0.5$). At stellar masses $>10^{11} M_\odot$, they occupy ≈30% of the sample (14/43). With the field correction, this implies a fraction of ≈20% and a surface density of dusty starburst galaxies of 0.86 ± 0.09 arcmin^2, which is 1.4 times that in the GOODS-N field. Eighteen of all the dusty starburst galaxies are detected at 24 μm, supporting the idea that they actually suffer from heavy dust obscuration. The median $\rm SFR_{UV,corr}$ and stellar mass of the dusty starburst galaxies are 92 $M_\odot$ yr^{-1} and 3.6×10^{10} $M_\odot$, respectively.

We also stacked the 24 μm images of the other 36 relatively isolated dusty starburst galaxies that were not individually detected. We find a $>3\sigma$ detection in the stacked image with a corresponding mean flux of 13 μJy. When limiting our stacking to a sample of 18 dusty galaxies that also satisfy the DRG color criterion, we also obtained significant 7.5σ detection with a mean flux of 48 μJy.

5. DISCUSSION

5.1. Quiescent Galaxies

The presence of quiescent galaxies at high redshift is very important for studying the history of massive galaxy formation in clusters. In the SSA22 protocluster, we detected 11 quiescent galaxies based on their $i' - K$ and $K - [4.5\,\mu{\rm m}]$ colors (Figure 4). All of these galaxies are also DRGs, showing strong Balmer or 4000 Å breaks between the observed J and K bands, large stellar masses, and low SFRs. Figure 6 shows the sky distribution of these quiescent galaxies. They are concentrated near the

Table 3
Number Counts of the Characteristic K-selected Galaxies at $2.6 < z_{\rm best} < 3.6$

Classification	Criterion	$N_{\rm obj}$[a]	Number Density (arcmin^{-2})	Ratio[b] (SSA22/field)
All the K-selected galaxies	$K < 24$	433(49)	3.87 ± 0.19	1.7 ± 0.1
	$M_{\rm star} > 10^{11}\,M_\odot$	43(11)	0.38 ± 0.06	1.8 ± 0.5
	$10^{10.5}\,M_\odot < M_{\rm star} < 10^{11}\,M_\odot$	116(7)	1.03 ± 0.10	1.6 ± 0.2
	$M_{\rm star} < 10^{10.5}\,M_\odot$	274(31)	2.45 ± 0.15	1.7 ± 0.2
Quiescent galaxies	$i' - K > 3$ & $K - [4.5\,\mu{\rm m}]$ & $K < 23$	11(1)	0.10 ± 0.03	...[c]
All of the 24 μm detected	$f_{24\,\mu{\rm m}} > 40\,\mu$Jy	31(5)	0.29 ± 0.05	...
24 μm detected	$f_{24\,\mu{\rm m}} > 100\,\mu$Jy	22(3)	0.20 ± 0.04	1.9 ± 0.7
Chandra full-band detected	$f_{0.5-8\,{\rm keV}} > 6 \times 10^{-16}$ erg cm^{-2} s^{-1}	19(10)	0.19 ± 0.04	2.5 ± 1.0
Chandra soft-band detected	$f_{0.5-2\,{\rm keV}} > 2 \times 10^{-16}$ erg cm^{-2} s^{-1}	14(8)	0.14 ± 0.04	2.4 ± 1.2
Chandra hard-band detected	$f_{2-8\,{\rm keV}} > 1 \times 10^{-15}$ erg cm^{-2} s^{-1}	13(8)	0.13 ± 0.04	3.4 ± 1.9
LAEs	$BV - NB497 > 1.2$ & $NB497 < 25.5$	9(5)	0.08 ± 0.03	6.8 ± 2.3[d]

Notes.
[a] Number of the K-selected galaxies at $2.6 < z_{\rm best} < 3.6$ ($2.6 < z_{\rm spec} < 3.6$).
[b] Ratio of the surface number density in the SSA22 protocluster compared with that in the general field. All the samples except for the LAEs are compared with those in the MODS in the GOODS-N field (Kajisawa et al. 2011). The LAEs are compared with those in the SXDS field (Ouchi et al. 2008; Ono et al. 2010).
[c] None of the K-selected galaxies at $2.6 < z_{\rm best} < 3.6$ in the GOODS-N field satisfy the color criterion of the quiescent galaxies.
[d] Ratio of the K-band detection rate of the LAEs in the SSA22 field and in the SXDS field.

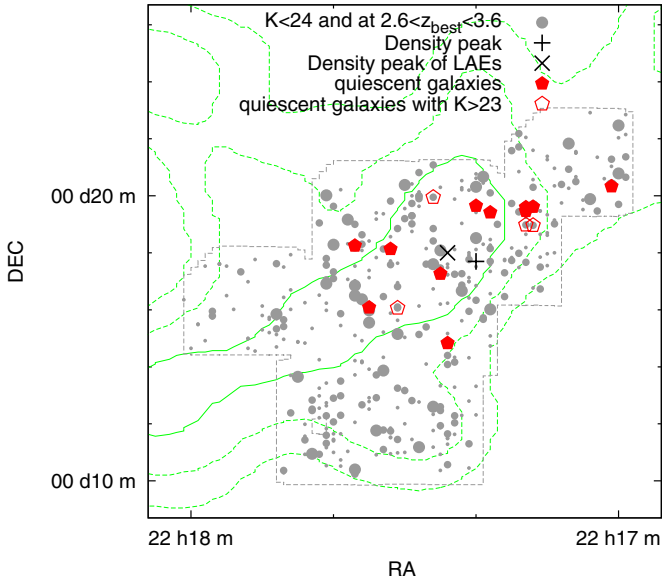

Figure 6. Sky distribution of the quiescent galaxies. The red filled pentagons are the quiescent galaxies selected as $i' - K > 3.0$, $K - [4.5\,\mu{\rm m}] < 0.5$, and $K < 23$ at $2.6 < z_{\rm best} < 3.6$. The open red pentagons are the K-selected galaxies at $2.6 < z_{\rm best} < 3.6$ that satisfy the color criterion of the quiescent galaxies but with $K > 23$. The gray filled circles are the galaxies with $K < 24$ at $2.6 < z_{\rm best} < 3.6$. The size of the symbols indicates the stellar masses of the galaxies, classified as $M_{\rm star} < 10^{10.5}\,M_\odot$ (small), $10^{10.5}\,M_\odot < M_{\rm star} < 10^{11}\,M_\odot$ (medium), and $M_{\rm star} > 10^{11}\,M_\odot$ (large). The green contours are the 1σ, 1.5σ, and 2σ density levels of LAEs (Hayashino et al. 2004). The cross shows the density peak of LAEs from Yamada et al. (2012) and the "X" shows the density peak of the K-selected galaxies at $2.6 < z_{\rm best} < 3.6$ estimated in Section 3.3.
(A color version of this figure is available in the online journal.)

density peak of protocluster LAEs and K-selected galaxies at $2.6 < z_{\rm best} < 3.6$. Such significant clustering of quiescent galaxies at $z \gtrsim 3$ has not been clearly shown before.

One of the quiescent galaxies in our sample was identified as a $z = 3.1$ LAE detected in the *Chandra* X-ray catalog, CXOSSA22 J221725.4+001717 (Hayashino et al. 2004; Lehmer et al. 2009b), at $z_{\rm spec} = 3.12$. The quoted redshift indicates that it is located in the outskirts of the protocluster or may belong to the field. The observed SED for this galaxy is well fit by an exponentially decaying SFR model with $\tau = 0.1$, an age of 0.72 Gyr, and $E(B-V) = 0.1$. We measured a stellar mass of $1.6 \pm 0.2 \times 10^{11}\,M_\odot$, a ${\rm SFR_{UV}} < 9.8 \pm 0.7\,M_\odot$ yr^{-1}, a dust-corrected ${\rm SFR_{UV,corr}} < 18.3 \pm 9.2\,M_\odot$ yr^{-1}, and a specific SFR of $\lesssim 10^{-10}$ Gyr^{-1}. The SED therefore indicates that the galaxy is quiescent. There are no significant AGN features based on rest-frame UV to optical indicators, as is often the case with massive galaxies at high redshift (Yamada et al. 2009). However, an AGN component may be responsible for its Lyα emission.

It is also interesting to study the structural properties of the quiescent galaxies. Although a detailed morphological study of $z \sim 3$ galaxies is beyond the capabilities of MOIRCS, we found that two of the quiescent galaxies were observed in existing archival *HST* data. Figure 7 shows the *HST* ACS-WFC3 and the MOIRCS images of these two quiescent galaxies. The top panels of the figure are the images of CXOSSA22 J221725.4+001717 discussed above. The object shown in the bottom panels is not spectroscopically confirmed but does show a 3σ excess in the $NB497$ narrowband Lyα emission. CXOSSA22 J221725.4+001717 is well resolved in the F160W observations. We fit the image with a Sérsic model (Sersic 1968) using the GALFIT software (Peng et al. 2002). We obtained Sérsic profile parameters of $r_e = 0.91 \pm 0.03$ kpc and $n = 4.51 \pm 0.51$. Such a profile is "de Vaucouleurs-like" and significantly compact, resembling the red compact massive galaxies observed at $z > 2$ in other recent papers (e.g., van Dokkum et al. 2008; Kriek et al. 2009; Gobat et al. 2012).

Papovich et al. (2012) and Zirm et al. (2012) reported the enhanced structural evolution of early-type galaxies in protoclusters at $z = 1.62$ and $z = 2.16$, respectively. Due to small-number statistics, confirming similar enhancements for the SSA22 protocluster would require additional high-resolution images, which are currently not available.

It is interesting to note that some of the quiescent galaxies are likely to be members of "multiple merging" systems (U12). U12 reported that about 40% of the LABs in the SSA22 field have multiple components in their extended Lyα emission. These components are therefore likely to be physically associated and

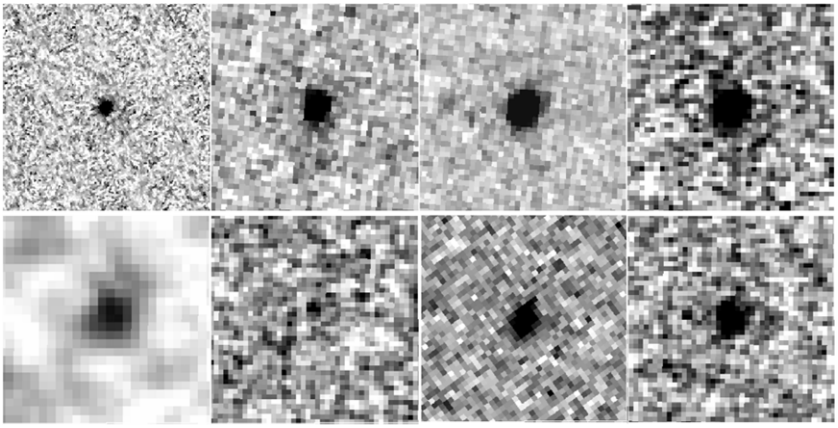

Figure 7. NIR images of the two quiescent galaxies covered by the *HST* WFC3 IR channel. The size of each image is 5.″0 on a side. The top panels are the *HST* ACS F814W, WFC3 F110W, F160W, and MOIRCS *K*-band images of CXOSSA22 J2217254-001717, from the left to the right. The bottom panels are the images of another quiescent galaxy that is only covered by F160W observations. The panels are Suprime-Cam i', MOIRCS *J*, *HST* WFC3 F160W, and MOIRCS *K* band, from left to right.

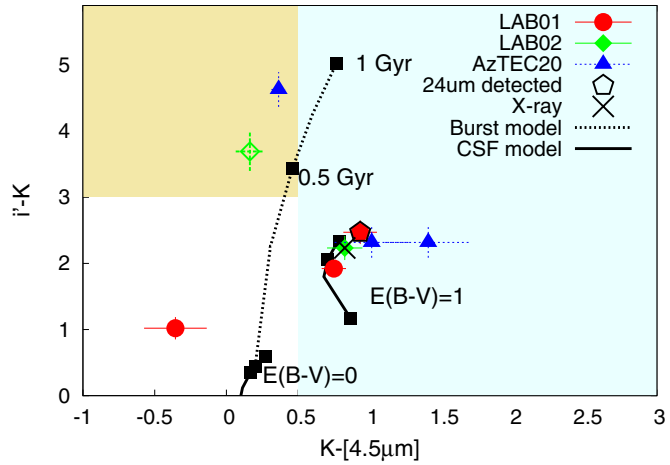

Figure 8. $i' - K$ versus $K - [4.5\,\mu\mathrm{m}]$ two color diagram, similar to Figure 4 but for the counterparts of two LABs and an ASTE/AzTEC sub-millimeter source. The red filled pentagons are the *K*- and [4.5 μm]-detected counterparts of LAB01, the green filled diamond is LAB02, and the blue filled triangles are the counterparts AzTEC20. The green open diamond is the counterpart of LAB02 with a slightly lower photometric redshift. The black pentagon is the galaxy detected in 24 μm and the black cross is the X-ray source. The models plotted here are the same as the Figure 4.

(A color version of this figure is available in the online journal.)

will merge with each other to form massive galaxies. The most significant cases, LAB01 and LAB02 (Matsuda et al. 2004), contain five and six massive components at $z_{\mathrm{phot}} \sim 3.1$ in their Lyα halos, respectively, which extend to scales larger than ~150 kpc. Furthermore, a sub-millimeter detected source AzTEC20 (Tamura et al. 2009) is also composed of 6 components with very red colors at $z_{\mathrm{phot}} \sim 3.1$ in the beam size of ASTE/AzTEC, $d \sim 20''$. The summed total stellar mass of the counterparts is larger than a few times $10^{11}\,M_{\odot}$ for each object.

Figure 8 shows the $i' - K$ and $K - [4.5\,\mu\mathrm{m}]$ colors for the *K*- and [4.5 μm]-band-detected counterparts of LAB01, LAB02, and AzTEC20. It appears that there are quiescent galaxies in LAB02 and AzTEC20, although the object in LAB02 has a photometric redshift slightly less than 2.6. The stellar masses of these quiescent galaxies are $7.3 \pm 0.5 \times 10^{10} M_{\odot}$ for the object in LAB02 and $5.6 \pm 0.2 \times 10^{11}\,M_{\odot}$ for the object in AzTEC20. The latter is already comparable to the most massive early-type galaxies in the present-day universe. There are also the galaxies with colors consistent with dusty starburst galaxies with $>5 \times 10^{10}\,M_{\odot}$ in the same groups. The quiescent galaxies in LAB02 and AzTEC20 may therefore experience major and minor mergers as the halo grows. At least some of the quiescent galaxies in the SSA22 protocluster have not been completely assembled and will experience further evolution.

5.2. The Dust-obscured Star Forming Galaxies

The enhancement of dusty starburst activity in the SSA22 protocluster was previously reported based on observations at sub-mm wavelengths (Geach et al. 2007; Tamura et al. 2009, 2010, 2013). Similarly, the density excess of red galaxies like DRGs and/or HEROs was previously reported by U12. One of the goals of this paper is to investigate the rest-frame UV to NIR colors of the protocluster galaxies to measure the density enhancement of the dusty starburst galaxies (Section 4.3). A large fraction of the DRGs and/or HEROs at $2.6 < z_{\mathrm{best}} < 3.6$ indeed show colors consistent with such dusty objects. We also found a density enhancement of 24 μm detected galaxies at $2.6 < z_{\mathrm{best}} < 3.6$, whose sky distribution is shown in Figure 9.

It remains uncertain whether 24 μm fluxes of the *K*-selected galaxies at $2.6 < z_{\mathrm{best}} < 3.6$ are typically from dusty starburst or AGN activity. Many sources detected at 24 μm have colors consistent with dusty starburst galaxies (Figure 4) and two thirds of these sources have $\mathrm{SFR_{UV,corr}} > 50\,M_{\odot}\,\mathrm{yr}^{-1}$. The entire sample of 24 μm-detected galaxies spans a wide range of SFR from 3 to 10,000 $M_{\odot}\,\mathrm{yr}^{-1}$, with a median value of 82 $M_{\odot}\,\mathrm{yr}^{-1}$. For comparison, their median stellar mass is $8.2 \times 10^{10}\,M_{\odot}$.

Three of the *K*-selected galaxies detected at 24 μm that have $2.6 < z_{\mathrm{best}} < 3.6$ are located within the beam size ($d \sim 20''$) of the ASTE/AzTEC sub-millimeter sources (Tamura et al. 2009). If we assume the IR SEDs are similar to local starburst galaxies (Dale & Helou 2002), the implied 1.1 mm flux of the galaxies with $f_{24\,\mu\mathrm{m}} = 100\,\mu$Jy would be 1–4 mJy, which is comparable to the 3σ detection limit of the ASTE/AzTEC observations (Tamura et al. 2009).

Two of the *K*-selected galaxies detected in 24 μm that have $2.6 < z_{\mathrm{best}} < 3.6$ happen to be covered by existing WFC3 F110W and F160W images. Figure 10 shows their ACS, WFC3, and MOIRCS *K*-band images. They clearly show extended and clumpy structures, which are quite different from quiescent red galaxies (see above). The structural properties of the six LBGs in the SSA22 protocluster were investigated by Mannucci

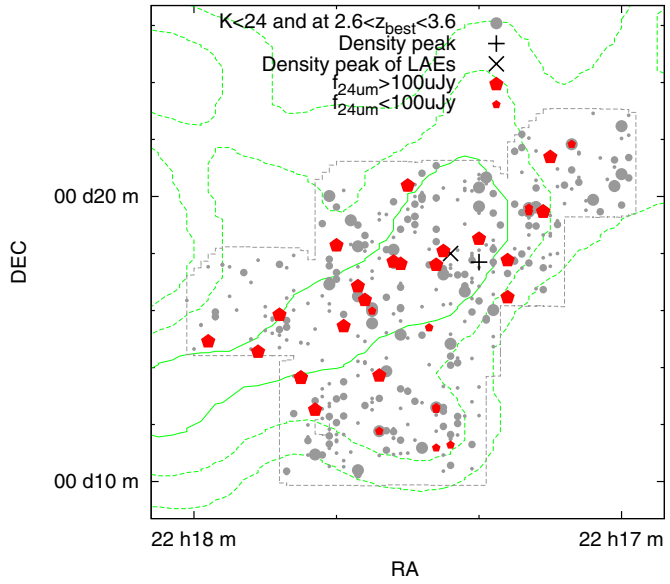

Figure 9. Similar to Figure 6 but for the *K*-selected galaxies detected at 24 μm at $2.6 < z_{\rm best} < 3.6$. The large red filled pentagons are the galaxies detected with $f_{24\,\mu{\rm m}} > 100$ μJy, the nominal detection limit at 24 μm. The small filled pentagons are the galaxies with 40 $\mu{\rm Jy} < f_{24\,\mu{\rm m}} < 100\,\mu{\rm Jy}$.

(A color version of this figure is available in the online journal.)

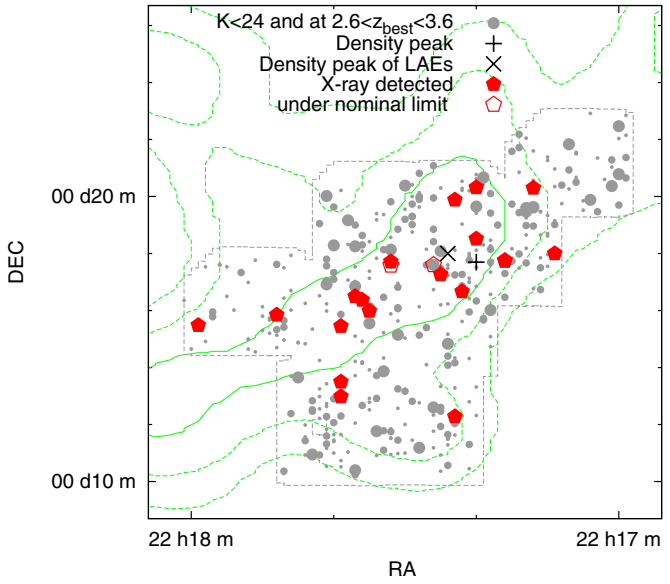

Figure 11. Similar to Figure 6 but for the *K*-selected galaxies detected in *Chandra* X-ray observations at $2.6 < z_{\rm best} < 3.6$. The red filled pentagons are the galaxies detected in *Chandra* full and/or soft and/or hard bands above the nominal detection limits. The open pentagons are the X-ray-detected galaxies but their X-ray fluxes are fainter than the nominal detection limits in the SSA22 field. Note that the M5 field was not covered with *Chandra* data.

(A color version of this figure is available in the online journal.)

et al. (2009) and Gnerucci et al. (2011). Compared with these LBGs, which also have SFRs $>50\,M_\odot$ yr^{-1}, stellar masses of $10^{10.3-11.3}\,M_\odot$, and relatively compact sizes (r_e = 1–2.5 kpc), the two 24 μm-detected objects have more extended and diffuse structures.

5.3. Active Galactic Nuclei

Figure 11 shows the sky distribution of the *K*-selected galaxies at $2.6 < z_{\rm best} < 3.6$ that are detected in the *Chandra* 0.5–8 keV band. Given the inferred luminosity limits over this redshift range, $L_{0.5-8{\rm keV}} > 3 \times 10^{42}$ erg s^{-1}, these X-ray-detected sources are almost certainly AGNs. The objects detected in the full (0.5–8 keV), soft (0.5–2 keV), and hard (2–8 keV) bands are plotted in Figure 11. The X-ray sources are clustered around the density peaks of the LAEs and *K*-selected galaxies at $2.6 < z_{\rm best} < 3.6$. Note that the *Chandra* data are relatively shallow over the M5 field. We therefore study the X-ray properties of galaxies within the 99.8 arcmin^2 area remaining after the exclusion of the M5 field. In this section, we discuss the number density of the X-ray sources, which are detected above the nominal detection limit in the SSA22 field (listed in Section 2). As seen in Figure 4, only a few of the X-ray detected sources have red $i' - K$ and blue $K - [4.5\,\mu{\rm m}]$ colors. This indicates that their *K*-band emission is not significantly affected by the [O III]$\lambda\lambda$5007 emission line shifted in *K* band.

The surface number densities of the *K*-selected galaxies at $2.6 < z_{\rm best} < 3.6$ associated with the X-ray sources are 0.19 ± 0.04 arcmin^{-2} in the full-band sample, 0.14 ± 0.04 arcmin^{-2} in the soft-band sample and 0.13 ± 0.04 arcmin^{-2} in the hard-band sample. These densities are 2.5 ± 1.0 times (full-band), 2.4 ± 1.2 times (soft-band), and 3.4 ± 1.9 times (hard-band) the corresponding X-ray source densities in the GOODS-N field. Since the number density of the entire sample of *K*-selected galaxies at $2.6 < z_{\rm best} < 3.6$ in the SSA22 field is 1.7 times that in the GOODS-N field (Section 3.3), the X-ray AGN hosting rate (i.e., the fraction of galaxies hosting an AGN) in the hard band is roughly twice that

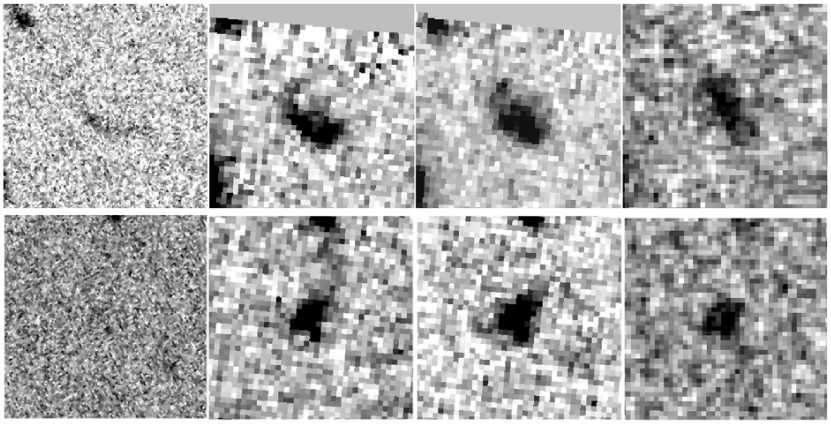

Figure 10. Similar to Figure 7 but for the 24 μm detected galaxies at $2.6 < z_{\rm phot} < 3.6$. The panels are *HST* ACS F814W, WFC3 F110W, F160W, and MOIRCS *K*-band images, from left to right.

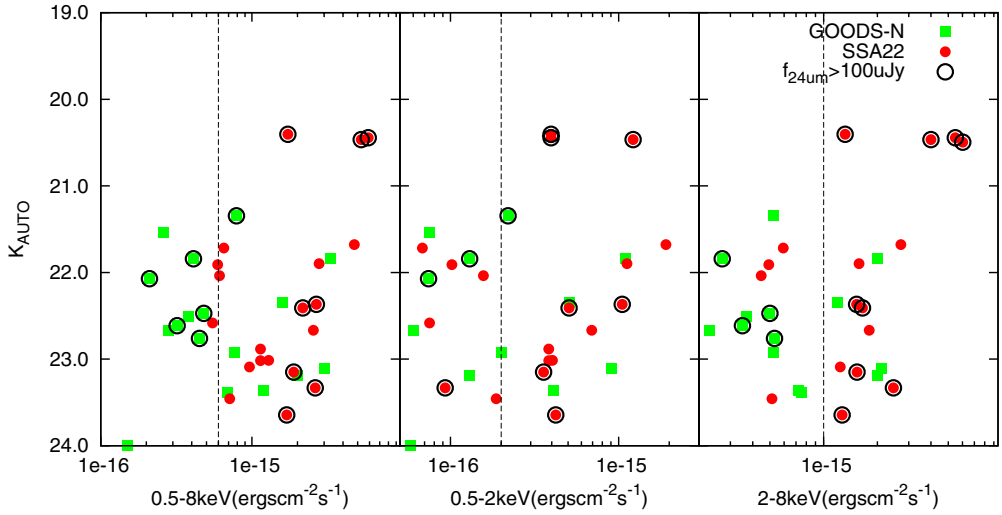

Figure 12. Total magnitudes in the *K* band versus fluxes in X-ray distributions for the *K*-selected galaxies at $2.6 < z_{\rm best} < 3.6$. The figures are full (0.5–8 keV), soft (0.5–2 keV), and hard bands (2–8 keV) from left to right. The red filled circles are the *K*-selected galaxies at $2.6 < z_{\rm best} < 3.6$ in the 99.8 arcmin^2 of the SSA22 field. The green filled squares are the *K*-selected galaxies at $2.6 < z_{\rm best} < 3.6$ in the 103.3 arcmin^2 in the GOODS-N field. The black circles are the objects with $f_{24\,\mu{\rm m}} > 100$ μJy. The dashed lines in each panel are the nominal detection limits of the *Chandra* data in the SSA22 field.

(A color version of this figure is available in the online journal.)

of the field. We note, however, that the statistical uncertainty here is large.

We plot *K*-band magnitudes versus the X-ray flux of the *K*-selected galaxies at $2.6 < z_{\rm best} < 3.6$ in Figure 12. In the GOODS-N field, there are only a few objects brighter than the nominal detection limits for the *Chandra* observations in SSA22. About half of the X-ray detected objects in SSA22 are also detected at 24 μm (>100 μJy). The AGNs in the SSA22 protocluster seem to be more powerful and more dust attenuated than those in the general field at similar redshifts. The 24 μm detection rate is largest for the hard-band sample, which is consistent with AGNs having large dust attenuations in the protocluster. The more luminous X-ray objects are observed in the SSA22 protocluster, which also suggests enhanced AGN activity.

There may be further contributions from a hidden population of dust-obscured AGNs that are faint in X-ray emission. Daddi et al. (2007) investigated 24 μm sources at $z > 2$ and found that the galaxies that are more luminous than $L_{8\mu{\rm m}} > 10^{11}\,L_\odot$ in νL_ν show a statistically significant X-ray detection when stacked. In the SSA22 field, among 31 *K*-selected galaxies at $2.6 < z_{\rm best} < 3.6$ detected at 24 μm, we find 10 that are also detected in the X-ray band. Since the detection limit in 24 μm in the SSA22 field corresponds to $L_{6\mu{\rm m}} \sim 10^{11} L_\odot$ in νL_ν, it is reasonable to expect that there are additional dust-obscured AGNs not detected in X-rays. Therefore, we consider the AGN hosting rate to be a lower limit.

The excess AGN hosting rate of LAEs and LBGs in the SSA22 protocluster was reported in Lehmer et al. (2009a, 2009b) and Webb et al. (2009). All the galaxies at $z_{\rm spec} \approx 3.09$ detected in X-rays listed in Table 1 of Lehmer et al. (2009b) lie in the MOIRCS observed area. All of them are also members of our *K*-selected sample. A similar enhancement was also reported for LAEs and BX/MD galaxies in the HS 1700+64 protocluster at $z = 2.30$ studied by Digby-North et al. (2010).

The excess AGN hosting rate of the galaxies in the SSA22 protocluster may be due to the enhanced activity of AGNs and/or the presence of more massive host galaxies in the protocluster environment. Given that supermassive black hole masses and their host galaxy stellar masses are tightly correlated in the local universe (e.g., Kormendy & Richstone 1995; Magorrian et al. 1998), it is possible that the enhanced AGN hosting rate is due to the presence of more massive galaxies there. In Table 3, we tabulate the surface number density of *K*-selected galaxies over three stellar mass ranges. The density excess in each stellar mass bin is similar to that of the whole *K*-selected galaxy sample. Therefore, at least, the excess AGN hosting rate of the *K*-selected galaxies at $2.6 < z_{\rm best} < 3.6$ is not likely to be simply due to the presence of more massive host galaxies in the SSA22 protocluster. The hard-band X-ray detection rates are $14 \pm 6\%$ in SSA22 and $9 \pm 6\%$ in GOODS-N for *K*-selected galaxies with $M_{\rm star} > 10^{11}\,M_\odot$ and $2.6 < z_{\rm best} < 3.6$. Further observations are needed to constrain how the protocluster environment influences AGN activity.

5.4. K-selected LAEs

A fraction of the *K*-selected galaxies at $2.6 < z_{\rm best} < 3.6$ show excesses in their $BV - NB497$ colors. Such excess colors are indicative of sources with either strong Lyα emission at $z \approx 3.09$ or [O II] emission at $z \approx 0.33$. The BV magnitude represents the average continuum flux at the wavelength of the narrowband (Hayashino et al. 2004). In fact, 41 out of the 433 *K*-selected galaxies show excesses in their narrowband flux above 4σ of the scatter in $BV - NB497$ color at each brightness. This criterion is less strict than that adopted to construct robust samples of LAEs (e.g., Hayashino et al. 2004); however, this result provides support that our photometric redshift measurements are reliable. In total, there are 78 robust $z = 3.1$ LAEs from Hayashino et al. (2004) that lie within the footprint of our MOIRCS observations. We find that 9 of these 78 LAEs are part of our *K*-selected sample.

Ono et al. (2010) explored the NIR properties of LAEs in the SXDS field; these findings can be compared with our results. In the SXDS field, only 5 out of the 224 LAEs at $z = 3.09$ in a 2340 arcmin^2 area were detected with $K < 24$ (3σ limit). Note that the narrowband filter used in their study, $NB507$, has a slightly different central wavelength but a similar bandwidth as that of $NB497$. The narrowband detection limit in SXDS varies from $NB507 = 25.1$ to 25.5 (5σ limit; Ouchi et al. 2008). All the LAEs detected in the *K* band in the SSA22

field have $NB497 < 25.1$, while the number of LAEs with $NB497 < 25.1$ (25.5) is 55 (69). Therefore, the *K*-band detection rate of the LAEs in the SSA22 protocluster (9/55 or conservatively, 9/69) is 5.8–6.8 times larger than that in the SXDS field (5/224).

The properties of the protocluster LAEs detected in the *K* band are also different from those of the LAEs in the SXDS field. The median stellar mass and stellar mass range of *K*-selected LAEs in SSA22 are $6.1 \times 10^{10} M_{\odot}$ and $10^{10-11} M_{\odot}$, respectively. In the SXDS field, these quantities are $\approx 3.7 \times 10^{9} M_{\odot}$ and $10^{9-10.5} M_{\odot}$, respectively. It has also been reported in other studies that rest-frame UV-selected galaxies like LBGs and LAEs in the protocluster are typically more massive than those in the general field (Steidel et al. 2005; Lehmer et al. 2009b; Digby-North et al. 2010; Matsuda et al. 2012). Furthermore, seven of the *K*-selected LAEs in the SSA22 protocluster satisfy the DRG color criterion, while there are no such objects in the SXDS field. Red LAEs have also been identified in other studies (Nilsson et al. 2007; Lai et al. 2008), but these sources are very rare. We caution that the red color could also be due to the contribution from a strong [O III]λλ5007 emission line. As discussed above, this is likely to be the case for two objects with $K > 23$, but the remaining seven brighter red LAEs are unlikely to be influenced by the [O III]λλ5007 emission line. We further note that four of the *K*-selected LAEs are also detected in *Chandra* X-ray observations.

The redshift evolution of the stellar populations of LAEs was reported by Nilsson et al. (2009), who found that LAEs at $z = 2.2$ are redder than those at $z = 3$. Nilsson et al. (2009) also reported a higher AGN fraction, more dust obscuration, and/or older stellar populations among the LAEs at $z = 2.2$ than those at $z = 3$. Our results indicate that the properties of LAEs at $z = 3$ are also strongly dependent upon environment.

The *K*-selected LAEs in the SSA22 protocluster are not low-mass analogs of LBGs. There are only two DRGs among the 26 LBGs at $z_{\rm spec} \approx 3.1$ that do not satisfy the robust LAE selection criteria. In this sense, our results are somewhat different from those of Lai et al. (2008), who investigated the $R - [3.6\,\mu{\rm m}]$ colors of LAEs and LBGs at $z \sim 3.1$ with deep IRAC 3.6 μm data. They argued that LAEs tend to be bluer in $R - [3.6\,\mu{\rm m}]$ than typical LBGs and are distributed within the extension of the faint and blue end of the LBG population.

6. CONCLUSIONS

We identified *K*-selected galaxies that are candidate members of the SSA22 protocluster at $z = 3.09$ using deep and wide NIR observations and photometric redshift fitting.

We found that the surface number density excess of *K*-selected galaxies at $2.6 < z_{\rm best} < 3.6$ in the SSA22 protocluster field is above that of the general field (e.g., from GOODS-N and GOODS-S). We also found that DRGs ($J - K < 1.4$) and 24 μm-detected galaxies among the *K*-selected population at $2.6 < z_{\rm best} < 3.6$ show even larger surface number density excesses. We identified 11 quiescent galaxies in our sample using their rest-frame UV to NIR colors. No such galaxies were identified throughout the entire GOODS-N field. Such significant clustering of the quiescent galaxies at $z \approx 3$ is reported here for the first time. Additionally, we found a density excess of dusty starburst galaxies selected by the color criterion, which indicates that the SSA22 protocluster galaxies are still experiencing enhanced star formation. There is also a density excess of *K*-selected galaxies at $2.6 < z_{\rm best} < 3.6$ detected in the X-ray bandpass. These sources are typically more obscured and X-ray luminous than those in the general field. Finally, we found an excess *K*-band detection rate for LAEs in the protocluster. Almost all of these LAEs are also DRGs. Such red LAEs are very rare in general fields.

From the above, we conclude that there is already a significant fraction of evolved quiescent massive galaxies in the SSA22 protocluster. However, star formation and also AGN activity is still ongoing and enhanced over the field. It appears that we are indeed witnessing a key formation epoch of elliptical galaxy formation in a protocluster that will collapse to form a rich galaxy cluster by $z = 0$.

We thank the MOIRCS Deep Survey team for providing the photometric and spectroscopic catalog in the GOODS-N field. We also thank Dr. Yoichi Tamura for providing the updated coordinates of the AzTEC sources. Our studies owe a great deal to the archival *Spitzer* IRAC & MIPS data taken from Webb et al. (2009), the *Chandra* data taken from Lehmer et al. (2009b), and the *HST* ACS and WFC3 data from proposal ID 11636 (PI Siana). This work was supported by the Global COE Program "Weaving Science Web beyond Particle-Matter Hierarchy," MEXT, Japan.

REFERENCES

Atek, H., Siana, B., Scarlata, C., et al. 2011, ApJ, 743, 121
Bertin, E., & Arnouts, S. 1996, A&AS, 117, 393
Blakeslee, J. P., Franx, M., Postman, M., et al. 2003, ApJL, 596, L143
Bolzonella, M., Miralles, J.-M., & Pelló, R. 2000, A&A, 363, 476
Bruzual, G., & Charlot, S. 2003, MNRAS, 344, 1000
Calzetti, D., Armus, L., Bohlin, R. C., et al. 2000, ApJ, 533, 682
Daddi, E., Alexander, D. M., Dickinson, M., et al. 2007, ApJ, 670, 173
Dale, D. A., & Helou, G. 2002, ApJ, 576, 159
Digby-North, J. A., Nandra, K., Laird, E. S., et al. 2010, MNRAS, 407, 846
Doherty, M., Tanaka, M., De Breuck, C., et al. 2010, A&A, 509, A83
Donley, J. L., Rieke, G. H., Pérez-González, P. G., Rigby, J. R., & Alonso-Herrero, A. 2007, ApJ, 660, 167
Elbaz, D., Hwang, H. S., Magnelli, B., et al. 2010, A&A, 518, L29
Ellis, R. S., Smail, I., Dressler, A., et al. 1997, ApJ, 483, 582
Franx, M., Labbé, I., Rudnick, G., et al. 2003, ApJL, 587, L79
Geach, J. E., Smail, I., Chapman, S. C., et al. 2007, ApJL, 655, L9
Gnerucci, A., Marconi, A., Cresci, G., et al. 2011, A&A, 528, A88
Gobat, R., Strazzullo, V., Daddi, E., et al. 2012, ApJL, 759, L44
Hatch, N. A., Overzier, R. A., Kurk, J. D., et al. 2009, MNRAS, 395, 114
Hayashino, T., Matsuda, Y., Tamura, H., et al. 2004, AJ, 128, 2073
Ichikawa, T., Suzuki, R., Tokoku, C., et al. 2007, PASJ, 59, 1081
Kajisawa, M., Ichikawa, T., Tanaka, I., et al. 2011, PASJ, 63, 379
Kajisawa, M., Kodama, T., Tanaka, I., Yamada, T., & Bower, R. 2006a, MNRAS, 371, 577
Kajisawa, M., Konishi, M., Suzuki, R., et al. 2006b, PASJ, 58, 951
Kakazu, Y., Cowie, L. L., & Hu, E. M. 2007, ApJ, 668, 853
Kennicutt, R. C., Jr. 1998, ARA&A, 36, 189
Kodama, T., Arimoto, N., Barger, A. J., & Arag'on-Salamanca, A. 1998, A&A, 334, 99
Kodama, T., Tanaka, I., Kajisawa, M., et al. 2007, MNRAS, 377, 1717
Kormendy, J., & Richstone, D. 1995, ARA&A, 33, 581
Kriek, M., van der Wel, A., van Dokkum, P. G., Franx, M., & Illingworth, G. D. 2008, ApJ, 682, 896
Kriek, M., van Dokkum, P. G., Labbé, I., et al. 2009, ApJ, 700, 221
Kuiper, E., Hatch, N. A., Röttgering, H. J. A., et al. 2010, MNRAS, 405, 969
Labbé, I., Huang, J., Franx, M., et al. 2005, ApJL, 624, L81
Lai, K., Huang, J.-S., Fazio, G., et al. 2008, ApJ, 674, 70
Le Floc'h, E., Papovich, C., Dole, H., et al. 2005, ApJ, 632, 169
Lehmer, B. D., Alexander, D. M., Chapman, S. C., et al. 2009a, MNRAS, 400, 299
Lehmer, B. D., Alexander, D. M., Geach, J. E., et al. 2009b, ApJ, 691, 687
Magdis, G. E., Rigopoulou, D., Huang, J.-S., & Fazio, G. G. 2010, MNRAS, 401, 1521
Magorrian, J., Tremaine, S., Richstone, D., et al. 1998, AJ, 115, 2285
Mannucci, F., Cresci, G., Maiolino, R., et al. 2009, MNRAS, 398, 1915
Matsuda, Y., Nakamura, Y., Morimoto, N., et al. 2009, MNRAS, 400, L66
Matsuda, Y., Richard, J., Smail, I., et al. 2010, MNRAS, 403, L54

Matsuda, Y., Smail, I., Geach, J. E., et al. 2011, MNRAS, 416, 2041
Matsuda, Y., Yamada, T., Hayashino, T., et al. 2004, AJ, 128, 569
Matsuda, Y., Yamada, T., Hayashino, T., et al. 2012, MNRAS, 425, 878
Mawatari, K., Yamada, T., Nakamura, Y., Hayashino, T., & Matsuda, Y. 2012, ApJ, 759, 133
Mayo, J. H., Vernet, J., De Breuck, C., et al. 2012, A&A, 539, A33
Meza, A., Navarro, J. F., Steinmetz, M., & Eke, V. R. 2003, ApJ, 590, 619
Moustakas, J., & Kennicutt, R. C., Jr. 2006, ApJS, 164, 81
Naab, T., Johansson, P. H., Ostriker, J. P., & Efstathiou, G. 2007, ApJ, 658, 710
Nilsson, K. K., Møller, P., Möller, O., et al. 2007, A&A, 471, 71
Nilsson, K. K., Tapken, C., Møller, P., et al. 2009, A&A, 498, 13
Ono, Y., Ouchi, M., Shimasaku, K., et al. 2010, ApJ, 724, 1524
Osterbrock, D. E. 1989, Astrophysics of Gaseous Nebulae and Active Galactic Nuclei (Mill Valley, CA: University Science Books)
Ouchi, M., Shimasaku, K., Akiyama, M., et al. 2005, ApJL, 620, L1
Ouchi, M., Shimasaku, K., Akiyama, M., et al. 2008, ApJS, 176, 301
Papovich, C., Bassett, R., Lotz, J. M., et al. 2012, ApJ, 750, 93
Papovich, C., Moustakas, L. A., Dickinson, M., et al. 2006, ApJ, 640, 92
Peng, C. Y., Ho, L. C., Impey, C. D., & Rix, H.-W. 2002, AJ, 124, 266
Pettini, M., Shapley, A. E., Steidel, C. C., et al. 2001, ApJ, 554, 981
Salpeter, E. E. 1955, ApJ, 121, 161
Sersic, J. L. 1968, Atlas de Galaxias Australes (Cordoba: Observatorio Astronomico)
Shapley, A. E., Steidel, C. C., Pettini, M., & Adelberger, K. L. 2003, ApJ, 588, 65
Steidel, C. C., Adelberger, K. L., Dickinson, M., et al. 1998, ApJ, 492, 428
Steidel, C. C., Adelberger, K. L., Shapley, A. E., et al. 2000, ApJ, 532, 170
Steidel, C. C., Adelberger, K. L., Shapley, A. E., et al. 2005, ApJ, 626, 44
Stetson, P. B. 1987, PASP, 99, 191
Tamura, Y., Iono, D., Wilner, D. J., et al. 2010, ApJ, 724, 1270
Tamura, Y., Kohno, K., Nakanishi, K., et al. 2009, Natur, 459, 61
Tamura, Y., Matsuda, Y., Ikarashi, S., et al. 2013, MNRAS, 430, 2768
Tanaka, I., Breuck, C. D., Kurk, J. D., et al. 2011, PASJ, 63, 415
Tokunaga, A. T., Simons, D. A., & Vacca, W. D. 2002, PASP, 114, 180
Toshikawa, J., Kashikawa, N., Ota, K., et al. 2012, ApJ, 750, 137
Totani, T., Yoshii, Y., Iwamuro, F., Maihara, T., & Motohara, K. 2001, ApJL, 558, L87
Uchimoto, Y. K., Suzuki, R., Tokoku, C., et al. 2008, PASJ, 60, 683
Uchimoto, Y. K., Yamada, T., Kajisawa, M., et al. 2012, ApJ, 750, 116
van Dokkum, P. G., Franx, M., Kriek, M., et al. 2008, ApJL, 677, L5
Venemans, B. P., Röttgering, H. J. A., Miley, G. K., et al. 2005, A&A, 431, 793
Webb, T. M. A., Yamada, T., Huang, J.-S., et al. 2009, ApJ, 692, 1561
Wuyts, S., Labbé, I., Franx, M., et al. 2007, ApJ, 655, 51
Yamada, T., Kajisawa, M., Akiyama, M., et al. 2009, ApJ, 699, 1354
Yamada, T., Nakamura, Y., Matsuda, Y., et al. 2012, AJ, 143, 79
Zirm, A. W., Toft, S., & Tanaka, M. 2012, ApJ, 744, 181
Zirm, A. W., van der Wel, A., Franx, M., et al. 2007, ApJ, 656, 66